Vertical profile of tropospheric ozone derived from synergetic retrieval using three different wavelength ranges, UV, IR, and Microwave: sensitivity study for satellite observation

Tomohiro O. Sato[1], Takao M. Sato[2,1], Hideo Sagawa[3], Katsuyuki Noguchi[4], Naoko Saitoh[5], Hitoshi Irie[5], Kazuyuki Kita[6], Mona E. Mahani[1,7], Koji Zettsu[1], Ryoichi Imasu[8], Sachiko Hayashida[4], and Yasuko Kasai[1,9]

[1]National Institute of Information and Communications Technology, Tokyo, Japan
[2]Institute of Space and Astronautical Science, Japan Aerospace Exploration Agency, Kanagawa, Japan
[3]Kyoto Sangyo University, Kyoto, Japan
[4]Nara Women's University, Nara, Japan
[5]Center for Environmental Remote Sensing, Chiba University, Chiba, Japan
[6]Ibaraki University, Ibaraki, Japan
[7]Tohoku University, Sendai, Japan
[8]Atmospheric and Ocean Research Institute, The University of Tokyo, Chiba, Japan
[9]Tokyo Institute of Technology, Tokyo, Japan

Correspondence to: Y. Kasai (ykasai@nict.go.jp)

Abstract. We performed a feasibility study of constraining the vertical profile of the tropospheric ozone by using a synergetic retrieval method on multiple spectra, i.e., ultraviolet (UV), thermal infrared (TIR) and microwave (MW) ranges, measured from space. A quantitative evaluation of the retrieval sensitivity of the tropospheric ozone by adding the MW measurement to the UV and TIR measurements was reported for the first time by this work. Two observation points in East Asia (one in an urban area and one in an ocean area) and two observation times (one during summer and one during winter) were assumed. Geometry of line-of-sight was nadir down-looking for the UV and TIR measurements, and limb-sounding for the MW measurement. The retrieval sensitivities of the ozone profiles in the upper troposphere (UT), middle troposphere (MT) and lowermost troposphere (LMT) were estimated using the degree of freedom for signal (DFS), the pressure of maximum sensitivity, reduction rate of error from the a priori error, and the averaging kernel matrix, derived based on the optimal estimation method. The measurement noise levels were assumed to be the same as those for currently available instruments. The weighting functions for the UV, TIR and MW ranges were calculated using the SCIATRAN radiative transfer model, the Line-By-Line Radiative Transfer Model, and the Advanced Model for Atmospheric Terahertz Radiation Analysis and Simulation, respectively. The DFS value was increased by approximately 96 %, 23 % and 30 % by adding the MW measurements to the combination of UV and TIR measurements in the UT, MT and LMT regions, respectively. The MW measurement increased the DFS value of the LMT ozone; nevertheless, the MW measurement alone has no sensitivity for the LMT ozone. The pressure of maximum sensitivity value for the LMT ozone was also increased by adding the MW measurement. These findings indicate that better information on LMT ozone can be obtained by adding constraints on the UT and MT ozone from the MW measurement. The results of this study are applicable to the upcoming air-quality monitoring missions, APOLLO, GMAP-Asia and uvSCOPE.

1 Introduction

The World Health Organization (WHO) estimates that around seven million people died as a result of the effects of air pollution in 2012 (WHO, 2014), and it cites air pollution as being one of the world's greatest environmental health risks. Ozone in particular adversely affects human health and agricultural production. Tropospheric ozone has been increasing globally at rates of 0.3–1.0 ppb yr^{-1} over past few decades in the northern hemisphere (Dentener et al., 2010, and references therein). Ozone is formed by sunlight-driven oxidation from ozone precursors such as methane (CH_4), carbon monoxide (CO), non-methane volatile organic compounds (NMVOCs), and nitrogen oxides (NO_x) in the troposphere. Monitoring of the amount of the tropospheric ozone is required to understand the current situation and to forecast future ozone amounts.

Ozone plays different roles in different altitude regions in the troposphere. It is well known that ozone at the surface level is a harmful pollutant that has a detrimental effect on the health of people and plants and that can significantly reduce crop yields. The lifetime of ozone in the free troposphere ranges from a few days to weeks, so the transport scale of ozone is potentially intercontinental and hemispheric. Upper tropospheric ozone is the third most important warming gas and is responsible for a large part of the human enhancement of the global greenhouse effect. For further understanding these different characteristics of tropospheric ozone, it is important to obtain information on the vertical distribution of ozone separately in the lowermost troposphere (LMT), in the middle troposphere (MT), and in the upper troposphere (UT) on a global scale.

Ozone has been observed from space in various spectral ranges, including the ultraviolet (UV), visible (VIS), thermal infrared (TIR), and microwave (MW) with different observation geometries (nadir-looking and limb-sounding). Observations at different wavelengths have sensitivity to ozone at different altitudes. Generally, nadir-looking observations in the UV/VIS range are sensitive to ozone in the LMT (e.g., the Ozone Monitoring Instrument, OMI, onboard the Aura satellite (Levelt et al., 2006) and the second Global Ozone Monitoring Experiment, GOME-2, onboard the MetOp satelle (Munro et al., 2006)), while nadir-looking in the TIR range is sensitive to ozone in the MT (e.g., the Thermal Emission Spectrometer, TES, onboard the Aura satellite (Osterman et al., 2008) and the Infrared Atmospheric Sounding Interferometer, IASI, onboard the MetOp satellites (Clerbaux et al., 2009)). Limb-sounding and stellar/solar-occultation is used to sound ozone in the stratosphere and above. Limb-sounding in the UV/VIS region sounds ozone in the stratosphere, and stellar occultation instruments observe ozone above the stratosphere (e.g., the Scanning Imaging Absorption Spectrometer for Atmospheric Chartography, SCIAMACHY, (Brinksma et al., 2006) and the Global Ozone Monitoring by Occultation of Stars, GOMOS, (Kyrölä et al., 2004) both onboard the Envisat satellite). Limb-sounding in the MW spectral range is sensitive at altitudes above the UT (e.g., the Microwave Limb Sounder, MLS, onboard the Aura satellite (Waters et al., 2006) and the Superconducting Submillimeter-Wave Limb-Emission Sounder, SMILES, onboard the International Space Station (Kikuchi et al., 2010)).

Measurement using several wavelength ranges is an advanced method of deriving a vertically resolved ozone profile. Ziemke et al. (2006) derived the global distribution of the tropospheric ozone column by subtracting the stratospheric ozone column measured using the MLS MW spectra from the total ozone column measured using the OMI UV spectra. A feasibility study of the tropospheric ozone profile retrieval using the optimal estimation method (OEM) (Rodgers, 2000) combining UV and TIR measurements was performed by Landgraf and Hasekamp (2007). Worden et al. (2007) implemented the concept of synergetic

retrieval using the OMI and TES measurements. Natraj et al. (2011) showed that retrieval sensitivity for the LMT is improved by combining the UV and TIR measurements. Fu et al. (2013) implemented a synergetic retrieval of boundary layer ozone using UV and TIR spectra measured with the OMI and TES instruments. The degree of freedom for signal (DFS) for ozone from the surface to 700 hPa was estimated to be 0.37±0.09 for 22 coincident measurements made using the OMI, the TES, and an ozonesonde from 2004 to 2008 (see Table 2 in Fu et al. (2013)). Cuesta et al. (2013) also performed a synergetic retrieval of boundary layer ozone, using the GOME-2 (for UV) and IASI (for TIR) measurements. The DFS values for ozone up to 3 km were estimated to be 0.34±0.04 and 0.23±0.04 over land and ocean, respectively, for 19–20 August 2009 over Europe (see Table 1 in Cuesta et al. (2013)). The corresponding heights of maximum sensitivity were 2.20±0.50 km and 3.42±0.59 km. The DFS values were increased by approximately 50 % by combining the GOME-2 and IASI measurements, compared with the IASI measurement alone. The other approach to retrieve the tropospheric ozone profile using neural network technique was performed with the SCIAMACHY nadir measurements for the UV and VIS ranges (Sellitto et al., 2012a, b). The results demonstrated the effectiveness of combining several wavelength ranges to retrieve the tropospheric ozone profile.

Our idea is to add MW measurements to improve the synergetic retrieval of the tropospheric ozone profile. To the best of our knowledge, no study has attempted to show how MW measurements improve the retrieval of the vertical profile of tropospheric ozone. In this study, we performed a feasibility study of obtaining a vertically resolved ozone amount in the troposphere by using synergetic retrieval from a combination of UV, TIR and MW measurements covering wide wavelength ranges. This work should be of benefit to future air-quality monitoring missions, such as Air POLLution Observation (APOLLO), Geostationary mission for Meteorology and Air Pollution (GMAP-Asia) (Kasai et al., 2011), uvSCOPE (Fujinawa et al., 2015), and air pollution prediction project in National Institute of Information and Communication Technology (NICT). The objective of the APOLLO and GMAP-Asia missions is to measure short-lived climate pollutants for monitoring global pollution and climate change. These missions assume atmospheric monitoring from the International Space Station (ISS) and from geostationary orbit, respectively. The uvSCOPE mission, a candidate for the earth observation section of ISS, aims to detect hot-spots of air pollutant with a high horizontal resolution (such as $1 \times 1 \, km^2$) for better understanding of the inventory of air pollution. The target of the NICT air pollution prediction project is to make health index to aid in the mitigation of air pollution disasters using high-horizontal resolution (a few km scale) pollution forecasting from multiple datasets, such as satellite observation, ground-based observation, and in-situ observation datasets.

In this paper, we report a feasibility study of the tropospheric ozone profile retrieval based on the concept of APOLLO, i.e., utilizing synergetic observation afforded by UV, TIR, and MW instruments to obtain vertically resolved information on tropospheric ozone not only at the boundary layer but also in the middle and upper troposphere. Our major aim of this feasibility study is to evaluate the sensitivity of the tropospheric ozone profile retrieval to the addition of the MW measurement to the multi-spectral synergetic retrieval. The simulation was thus performed under ideal conditions for synergetic retrieval of the tropospheric ozone profile.

2 Observation scenario

2.1 Observation wavelength region and geometry

The observation scenario used in the simulation follows the concept of the APOLLO mission. Three spectrometers in the ISS were assumed to observe the three wavelength ranges: UV, TIR, and MW. Figure 1 shows the observation geometries for the three spectrometers. The UV and TIR instruments used nadir down-looking, and the MW one used limb-sounding at tangent heights from 10 to 80 km. In this feasibility study, we assumed spherically homogeneous atmosphere along the line-of-sight of the MW measurement. The height of the ISS was assumed to be 300 km. The azimuthal direction of the field-of-view of the MW limb-sounding was set parallel to the ISS's orbital motion. The tangent point of the MW limb-sounding passes the UV and TIR nadir down-looking point approximately five minutes before the UV and TIR nadir down-looking. The time delay of 5 minutes corresponds to approximately 6 km travel if a typical value of horizontal wind speed in the troposphere and the stratosphere (1.2 km/min) is assumed (Fleming et al., 1988), which is less than the typical horizontal resolution of the MW limb measurement (8 km for Aura/MLS (Waters et al., 2006)). Therefore, we ignored this time difference between the UV and TIR measurements and MW measurement. Table 1 summarizes the specifications of the three instruments and the three radiative transfer models.

The wavelength range for the UV measurement was set to 305–340 nm. UV wavelength range shorter than 305 nm is useful for the stratospheric ozone profile retrieval (e.g., Bak et al., , 2012). We added the MW limb measurement which is more sensitive to stratospheric ozone. We excluded the shorter UV wavelength ranges to clearly show whether stratospheric ozone profile retrieval using MW measurement improves the sensitivity of tropospheric ozone profile retrieval. Although there is a benefit of adding VIS wavelengths (340–505 nm) (e.g., Sellitto et al., 2012a, b), we decided not to because the wavelength dependence of surface reflectance, the absorption of NO_2, and the Ring effect were beyond the scope of this study. The spectral resolution, defined as the full width at half maximum (FWHM), and the sampling step were assumed to be 0.6 nm and 0.2 nm, respectively. The noise equivalent spectral radiance (NESR) was obtained by dividing the simulated backscattered radiance by the signal-to-noise ratio (SNR). We used SNR values of the APOLLO instrument setups in the UV simulation. Three references of the SNR value were prepared for high, middle and low level of the radiance. The SNR value for the simulated radiance was linearly interpolated by the two of three reference SNR values. Table 2 shows the reference SNR values at 305 nm and 340 nm, and the solar zenith angle (SZA) and surface albedo of the three conditions [Private communication with K. Gerilowski]. The values of SNR used in the UV simulation were estimated to be approximately 90 and 1400 at 305 nm and 340 nm, respectively.

We assumed that the nadir-viewing TIR instrument was a Fourier transform spectrometer covering the TIR spectral range (980–1080 cm^{-1}) including the ozone v3 absorption band, 9.6 μm (1045 cm^{-1}) as TES (Osterman et al., 2008) and IASI (Clerbaux et al., 2009). We set the maximum optical path difference to 8.33 cm, which corresponds to a spectral resolution of 0.12 cm^{-1} and calculated the noise equivalent differential temperature for each wavelength, assuming that the SNR is a constant value of 300 over the entire spectral range.

Several ozone transitions in the microwave/submillimeter range have been employed by recent space-borne instruments, e.g., 206.1 and 235.7 GHz for Aura/MLS (Waters et al., 2006), 501.8 and 544.6 GHz for Odin/SMR (Urban et al., 2005), and

625.4 GHz for Aura/MLS and JEM/SMILES (Kikuchi et al., 2010). The assumed MW limb-sounding instrument covered two frequency bands: the 350 GHz band (345–357 GHz) and the 645 GHz band (639–651 GHz). There are ozone lines at 352.3, 352.8, and 355.0 GHz in the former and at 640.1, 642.3, 644.8, 645.6, 647.8, and 650.7 GHz in the latter. These frequency bands were selected for detection of not only ozone but also other molecules related to global warming and air-pollution (H_2O, CO, CH_3CN, N_2O, SO_2, H_2CO, and HNO_3). The channel separation width of the spectrometer was assumed to be 25 MHz. The frequency resolution, defined by FWHM was set to be identical to the channel separation width. The antenna diameter was assumed to be 40 cm. The Earth's limb was assumed to be scanned vertically from 10 to 80 km with an interval of 2 km and total 35 spectra were acquired in one vertical limb scan. We assumed that the typical integration time was 0.5 seconds for one spectrum accumulation and that it took 17.5 seconds for one vertical limb scan. The brightness temperature noise was estimated to be 0.7 K and 1.7 K for the 350 GHz and 645 GHz bands, respectively, assuming the system noise temperature of a typical Schottky-barrier mixer (2500 K and 6000 K for the 350 GHz and 645 GHz bands, respectively).

2.2 Atmospheric conditions

We used typical atmospheric scenarios in summer and winter for East Asia, which is one of most ozone-polluted regions and a major source of the intercontinental transport of ozone toward North America. We chose two observation points in East Asia, 35°N, 116.5°E (Central-East China, CEC, located between Beijing and Shanghai) and 31°N, 127.25°E (East China Sea, ECS, centered among China, Japan, South Korea, and Taiwan). The CEC is the area where largest amount of the boundary layer ozone was observed from the Aura/OMI measurement (Hayashida et al., 2015). The ECS was chosen for a comparison of urban area and ocean. We selected June and December for representatives of summer and winter seasons, respectively. Hayashida et al. (2015) reported the amount of the boundary layer ozone in the area near CEC was maximized in June and minimized in December. The observation time was set to 04:00am GMT, which corresponds to 11:46am and 00:29pm for CEC and ECS local times, respectively. The local times around noon were set because ozone profile retrieval sensitivity is apparently higher when the solar zenith angle (SZA) is low or moderate, as shown in a simulation study by Landgraf and Hasekamp (2007).

We made a total of 20 atmospheric scenarios, as shown in Table 3. The vertical profiles of ozone, temperature and water vapor are shown in Figure 2. Of the four cases (CEC in June, ECS in June, CEC in December, and ECS in December), the ozone partial column (PC) in the LMT was the largest (approximately 5×10^{21} m^{-2}) for CEC in June and was the smallest (approximately 2×10^{21} m^{-2}) for CEC in December.

We interpolated the values of ozone, temperature and water vapor from the following three original atmospheric profiles by using cubic splines to make the atmospheric profile smooth in the overlapping regions for a vertical pressure (p) grid defined as follows.

$$p[i] = \begin{cases} 10^{3-(i+1)/24} \, [\text{hPa}] & i = 1, 2, \ldots, 71 \ (\geq 1\,\text{hPa}) \\ 10^{3-(i-35)/12} \, [\text{hPa}] & i = 72, 73, \ldots, 108 \ (< 1\,\text{hPa}) \end{cases}$$

The scale height of the vertical profiles that we used was 3 km.

The profiles of ozone, temperature, and water vapor in the vertical region from the surface to 65 hPa (approximately 20 km) were simulated by a one-way nested global-regional air quality forecasting (AQF) system (Takigawa et al., 2007, 2009). This system is based on the CHASER (Chemical Atmospheric General Circulation model for the Study of Atmospheric Environment and Radiative Forcing) model (Sudo et al., 2002) and the WRF (Weather Research and Forecasting)/Chem model (Grell et al.,

5   2005) version 3.3. The horizontal resolution of this system is approximately 40 km. The profiles over CEC and ECS were spatially averaged for the periods of June 1 to June 30 and December 1 to December 31, 2009. The surface temperature was simulated with the AQF system; the temperature difference between the surface and the lower boundary of the lowest atmospheric layer was less than 1 K. We set the surface temperature equal to the value at surface pressure since the effect of the temperature contrast between the atmosphere and surface is large for the TIR measurement.

10   The profiles (ozone, temperature and water vapor) for the 985–0.01 hPa vertical range were taken from the Modern Era Retrospective-Analysis for Research and Applications (MERRA) data (Rienecker et al., 2011). The "MERRA DAS 3d ana-lyzed state (inst6_3d_ana_Nv)" data product provided three-dimensional fields for layer pressure thickness, air temperature, specific humidity, and ozone mixing ratio at six-hour intervals (00:00, 06:00, 12:00, 18:00 GMT). The MERRA data covered a $0.66° \times 0.5°$ latitude-longitude grid. We averaged the MERRA data at 06:00 GMT (the closest local time of 12:00 LT in CEC

15   and ECS) on the same date of the selected AQF system profiles for each region (CEC and ECS). No interpolation for local time was performed on the MERRA data.

The temperature data of the COSPAR International Reference Atmosphere (CIRA) model (Fleming et al., 1990) was used above the vertical level of 0.01 hPa. The CIRA-86 model includes monthly and zonally mean temperatures and pressures (0–120 km) with almost global coverage (80°N–80°S) at an interval of 10°. We averaged the two temperature data at 30°N and

20   40°N for CEC, and used the temperature data at 30°N for ECS. The mixing ratios of ozone and water vapor at pressures less than 0.01 hPa were assumed to be equal to those at the upper boundary (0.01 hPa) of the MERRA data due to the lack of appropriate reference data. We confirmed that the effects of the assumption for the upper vertical range were negligibly small for our calculation.

We assumed the following quasi-clear sky cases for all scenarios. A no-cloud condition was considered for all wavelength

25   ranges. Basic background aerosol was taken into account only in the UV calculation. The aerosol profile was included as a known parameter because it was reported that the inclusion of aerosol profile changed within 2 % of the LMT ozone amount in case of the Aura/OMI measurement (Hayashida et al., 2015). We used the vertical profiles of urban and maritime aerosols of a standard mixing state as described by Hess et al. (1998). These profiles were adjusted to be 0.2 of the total optical thicknesses of the aerosols (moderate pollution). The aerosol profile was not included in the TIR calculation because the

30   extinction of radiation due to aerosol particles with a scale of approximately 9.6 μm, which corresponds to the wavelength of the TIR range, is negligibly small for the synergetic retrieval of the LMT ozone with the TIR measurement (e.g., Natraj et al., 2011). We assumed that surface albedo was constant in the target UV range (305–340 nm). The information on surface albedo for simulating UV radiance spectra was taken from the database described by Kleipool et al. (2008). This database contains the monthly global maps of the Earth's surface Lambertian equivalent reflectance (LER) deduced from the Aura/OMI

35   measurements. We obtained monthly and spatially averaged albedo values of 0.056 (June) and 0.063 (December) for CEC

6

and 0.065 (June) and 0.084 (December) for ECS, respectively, from the LER data at the wavelength of 328.1 nm, which is the shortest wavelength in the database. The effect of the uncertainty of the UV surface albedo on tropospheric ozone measurements from space was discussed by Noguchi et al. (2014). The surface emissivity for modeling the TIR radiance spectra was estimated by linear regression analysis based on the Advanced Space-borne Thermal Emission Reflection Radiometer (ASTER) Spectral Library (Baldridge et al., 2009). The surface emissivity for the MW measurement was set to 1.0 for the entire range. MW limb measurements are generally insensitive to the surface emissivity since the atmosphere is strongly opaque in this wavelength range.

3   Synergetic retrieval simulation

3.1   Forward models of UV, TIR, and MW regions

We used the SCIATRAN radiative transfer model version 3.1 (Rozanov et al., 2005), the Line-By-Line Radiative Transfer Model (LBLRTM) version 12.1 (Clough et al., 2005), and the Advanced Model for Atmospheric Terahertz Radiation Analysis and Simulation (AMATERASU) (Baron et al., 2008) for the calculation of spectra in the UV, TIR, and MW wavelength ranges, respectively. To investigate the potential advantage of including MW observations in the retrieval of the tropospheric ozone profile, we assumed no bias between the three forward models.

The SCIATRAN model was developed by the Institute of Remote Sensing/Institute of Environmental Physics (IFE/IUP) of the University of Bremen, Germany, for fast and precise simulation of radiance spectra in the UV, VIS and near infrared ranges as measured by spaceborne instruments, e.g., GOME (240–790 nm) and SCIAMACHY (240–2400 nm). SCIATRAN is applicable to spectral regions ranging from 175.44 nm to 2400 nm, and is basically compatible with arbitrary observation geometries and sensor positions in space, in the atmosphere, and on the ground. The spherical shape of the Earth's atmosphere, including the refraction effect, is properly taken into account when simulating the radiance spectra.

The LBLRTM model is an accurate and efficient line-by-line radiative transfer model and has been extensively validated for atmospheric radiance spectra from UV to submillimeter-wave ranges. The line-by-line calculation of the optical thickness of the atmospheric layers is conducted on the basis of the spectroscopic line parameter database (HITRAN 2008) with its updates (Rothman et al., 2009). This model is used as the forward model in retrieval algorithms for analyzing spaceborne measurements such as EOS-Aura/TES (Clough et al., 2006), and GOSAT/TANSO-FTS (Saitoh et al., 2009).

The AMATERASU model consists of a line-by-line radiative transfer calculation allowing for a multi-layered horizontally homogeneous shell atmosphere. This model has been implemented in the retrieval analysis of the SMILES measurements (e.g., Baron et al., 2011) and in the feasibility study of a submillimeter instrument for planetary science (Kasai et al., 2012). The spectroscopic parameters were from commonly used databases such as the HITRAN 2008 molecular spectroscopic database (Rothman et al., 2009) and the JPL spectroscopic catalog (Pickett et al., 1998). The continuum absorption due to dry and wet air was taken into account; it is based on the formulation in Pardo et al. (2001).

3.2 Theoretical retrieval basis and error estimation

The optimal estimation method (OEM) (Rodgers, 2000) was used for the synergetic retrieval and error estimation. The retrieved state vector $\hat{x}$ was estimated by minimizing the differences between the observed radiance spectra y_{obs} and the modeled radiance spectra y_{mod}, using a constraint from an a priori state vector x_{a}.

$$\hat{x} = Ax + (I - A)\,x_{\mathrm{a}} + G\epsilon \tag{1}$$

In this equation, x is the true state vector, A is the averaging kernel matrix, G is the gain (contribution function) matrix, and ϵ is the measurement noise vector. The averaging kernel matrix characterizing the sensitivity of the retrieved state vector $\hat{x}$ to the true state vector x is given by

$$A = \frac{\partial \hat{x}}{\partial x} = GK = \left(K^T S_\epsilon^{-1} K + S_{\mathrm{a}}^{-1}\right)^{-1} K^T S_\epsilon^{-1} K, \tag{2}$$

where S_{a} and S_ϵ are the a priori covariance matrix and the measurement error covariance matrix, respectively. K is a weighting function matrix ($K = \partial y_{\mathrm{mod}}/\partial x$). A corresponds to the identity matrix when the retrieved profile is equal to the true atmospheric profile. The number of state vector elements that are independently resolved is obtained by summing the diagonal elements of A, and is defined as DFS. The ith element of measurement response vector, $m[i]$, is defined as

$$m[i] = \sum_j A[i,j]. \tag{3}$$

A value of the measurement response element near unity indicates that almost all information in the retrieval result comes from the observation spectra, while a small value indicates that the retrieval result is largely affected by the a priori.

The total retrieval error covariance $\hat{S}$ is calculated using the covariance matrices of the smoothing error S_{s} and measurement noise S_{m}.

$$\begin{aligned}
\hat{S} &= S_{\mathrm{s}} + S_{\mathrm{m}} \\
&= (I - A)\,S_{\mathrm{a}}\,(I - A)^T + GS_\epsilon G^T \\
&= \left(K^T S_\epsilon^{-1} K + S_{\mathrm{a}}^{-1}\right)^{-1} \tag{4}
\end{aligned}$$

The square root of the $\hat{S}$ diagonals is the total retrieval error in $\hat{x}$ (ϵ_x). The value of ϵ_x at the ith layer is given by

$$\epsilon_x[i] = \sqrt{\hat{S}[i,i]}. \tag{5}$$

We evaluated the sensitivity of the vertical profile of ozone from the synergetic retrieval for seven different combinations of the wavelength ranges, i.e., UV, TIR, MW, TIR+MW, UV+MW, UV+TIR and UV+TIR+MW, in the 20 atmospheric scenarios. The state vectors x, $\hat{x}$ and x_{a} were calculated using logarithm units of the volume mixing ratio (VMR). The diagonal components of S_{a} were the squares of the a priori error σ_{a} at each vertical pressure grid). The value of σ_{a} was set to 100 % of the log-based a priori VMR to simply quantify the error reduction from the error in the a priori error to the error in the retrieved state. The off-diagonal components in S_{a} indicate the correlations between the ozone concentrations in different vertical layers.

The non-zero off-diagonal components in S_a facilitate retrieval of the ozone concentration in a layer for which sufficient ozone information is not included in the measurement spectrum with the correlations with other layers in which sufficient ozone information is included in a measurement spectrum (e.g., Saitoh et al., 2009). We set the off-diagonal components in S_a to zero to avoid the assistance of the ozone profile retrieval by the correlations between different vertical layers. The diagonal components of S_ϵ were the squares of the measurement error σ_ϵ. The off-diagonal components of S_ϵ were set to zero.

We normalized the state vector x and measurement vector y with σ_a and σ_ϵ because values of different order in a vector and a matrix often cause undesirable mathematical errors.

$$u = \frac{x - x_a}{\sigma_a} \tag{6}$$

$$v = \frac{y_{\text{obs}} - y_{\text{mod}}}{\sigma_\epsilon} \tag{7}$$

The normalized weighting function is given by

$$K' = KD\left(\sigma_a/\sigma_\epsilon\right). \tag{8}$$

Here, $D(a)$ is a diagonal matrix in which the diagonal elements are equal to the components of the vector a. S_a and S_ϵ were normalized in the same way.

$$S'_a = D\left(1/\sigma_a\right) S_a D\left(1/\sigma_a\right)^T \tag{9}$$

$$S'_\epsilon = D\left(1/\sigma_\epsilon\right) S_\epsilon D\left(1/\sigma_\epsilon\right)^T \tag{10}$$

A and $\hat{S}$ are expressed using the normalized vectors and matrices as

$$A' = \left(K'^T S'^{-1}_\epsilon K' + S'^{-1}_a \right)^{-1} K'^T S'^{-1}_\epsilon K', \tag{11}$$

$$\hat{S}' = \left(K'^T S'^{-1}_\epsilon K' + S'^{-1}_a \right)^{-1}. \tag{12}$$

We evaluated the sensitivity of ozone profile retrieval for seven wavelength combinations in terms of DFS. We calculated the DFS values for the partial column in the UT, MT and LMT regions. The value of DFS from the i_{min}th vertical layer to the i_{max}th layer is given by

$$\text{DFS} = \sum_{i=i_{\text{min}}}^{i_{\text{max}}} A[i,i]. \tag{13}$$

We also evaluated the sensitivity of ozone profile retrieval using the pressure of maximum sensitivity (PMS) and the reduction rate of error (RRE) for the partial column. The PMS was defined as the pressure of the maximum of the sum of rows of the corresponding A for the ozone partial column. The RRE is given by

$$\text{RRE} = \frac{\text{PCE}_{\text{apriori}} - \text{PCE}_{\text{retrieved}}}{\text{PCE}_{\text{apriori}}} \quad [\%] \tag{14}$$

where $\text{PCE}_{\text{apriori}}$ and $\text{PCE}_{\text{retrieved}}$ are the partial column error, PCE, for the a priori state and the retrieved state, respectively. PC represents the partial column of ozone, and the value of PC from the i_{min}th vertical layer to the i_{max}th layer is given by

$$\text{PC} = \sum_{i=i_{\text{min}}}^{i_{\text{max}}} \frac{p[i] \cdot \text{VMR}[i]}{k_{\text{B}} \cdot T[i]} \Delta z[i]. \tag{15}$$

Here, $p[i]$, VMR$[i]$, $T[i]$ and $\Delta z[i]$ are pressure, VMR of ozone, temperature, and the vertical length of the ith layer, respectively. k_B is the Boltzmann constant. The PCE is given by

$$\mathrm{PCE} = \sum_{i=i_\mathrm{min}}^{i_\mathrm{max}} \frac{p[i] \cdot \epsilon_\mathrm{VMR}[i]}{k_\mathrm{B} \cdot T[i]} \Delta z[i]. \tag{16}$$

$\epsilon_\mathrm{VMR}[i]$ is the total retrieval error in the ozone VMR at the ith layer (σ_a for PCE$_\mathrm{apriori}$ and $\epsilon_{\boldsymbol{x}}$ for PCE$_\mathrm{retrieved}$).

5 ## 4   Results and discussion

The sensitivities of ozone profile retrieval in terms of DFS (calculated using Eq. (13)) are plotted in Fig. 3 and summarized in Table 4. The average DFS values are plotted in red for CEC in June, in purple for ECS in June, in green for CEC in December, in blue for ECS in December, and in black for all 20 profiles. The error bars represent the standard deviation.

The DFS values in the UT region averaged for all 20 profiles were calculated to be 0.16±0.08, 0.59±0.10 and 0.44±0.41
10 for the UV, TIR, and MW wavelength range, respectively. None of the average DFS values for one wavelength range was larger than unity. For multiple-wavelength measurement, the DFS values increased to 1.15±0.25, 0.90±0.30, 0.62±0.08, and 1.21±0.28, for the TIR+MW, UV+MW, UV+TIR, and UV+TIR+MW measurement combinations, respectively. The DFS for the UV+TIR combination was the lowest among the four multiple-wavelength measurements; adding the MW measurement approximately doubled the DFS value. The addition of the MW measurement was thus the most effective way of
15 improving the retrieval of the ozone profile in the UT region.

In the MT region, the TIR measurement was the main contributor of DFS information. The DFS values were 0.50±0.16, 0.83±0.11, and less than 0.01 for the UV, TIR and MW wavelength ranges, respectively. The DFS values increased in the same way as in the UT calculation by adding measurements in different wavelength ranges. The average DFS values for the 20 profiles were 1.03±0.09, 0.73±0.09, 1.00±0.09 and 1.23±0.13 for TIR+MW, UV+MW, UV+TIR and UV+TIR+MW,
20 respectively. It should be noted that, although the MW measurement provided no information on ozone in the MT region because of atmospheric opacity, it nevertheless increased the DFS in the MT region from 1.00 to 1.23 (approximately 23 %) for the TIR+UV measurement. This indicates that information on ozone in the stratosphere and UT, where the sensitivity of the MW measurement is high, is also important for retrieval of the ozone profile for the MT region.

The DFS values in the LMT region were generally smaller than those in the UT and MT regions. They were calculated
25 to be 0.20±0.13, 0.21±0.15, less than 0.01, 0.20±0.14, 0.26±0.15, 0.46±0.25 and 0.60±0.27 for UV, TIR, MW, TIR+MW, UV+MW, UV+TIR and UV+TIR+MW, respectively. The DFS values of the UV and TIR wavelength ranges were almost the same, while the MW measurements had no sensitivity in the LMT region. Similar to that in the MT region, the DFS value for the UV+TIR measurement (0.46) increased to 0.60 (about 30 %) as a result of adding the MW measurement. We note that the DFS value for the TIR measurement for ECS in December was larger than that for the TIR+MW measurement. The averaging
30 kernel matrix in the LMT region for the TIR measurement in this case was discontinuously large. Since discontinuity generally occurs in the averaging kernel due to mathematical factors, not atmospheric physical factors, we do not discuss the DFS value for the TIR measurement in the ECS in December case.

We compared our results with those of previous studies of estimating the tropospheric ozone sensitivity using DFS. The DFS values for UV, TIR and UV+TIR measurements are summarized in Table 5. Since the scenarios of the simulation or measurement are different among this work and the previous studies, the DFS values cannot be directly compared. We thus calculated the relative differences between the DFS values for the UV+TIR measurements and the mean of the DFS values for the UV and TIR measurements. The relative difference for our simulation for all profiles averaged was 126 %, which shows good agreement with those of Fu et al. (2013) (139 %), Cuesta et al. (2013) (104 %) and Natraj et al. (2011) (115 %).

The pressure of maximum sensitivity, PMS, for the ozone partial column should be located within the corresponding vertical region. The PMS values for the UT calculation for all cases were located within the corresponding range (215–383 hPa) when two or more wavelength ranges were combined. This was also observed for the MT calculation. For the LMT calculation, this was observed only when three wavelength ranges were combined. The PMS values for all profiles averaged for the LMT were 783 hPa and 808 hPa for the UV+TIR and UV+TIR+MW measurements, respectively. The PMS value was increased approximately 3 % by adding the MW measurement to the combined UV+TIR measurement although the PMS value in the MW measurement for the LMT was lower than 300 hPa.

The reduction rate of error, RRE, for the partial column of ozone calculated using Eq. (14) is shown on the right in Fig. 4. The RRE was approximately 0–20 % in the UT, MT and LMT regions. It was generally higher when more wavelength ranges were combined in the ozone synergetic retrieval, as shown by the DFS values plotted in Fig. 3. The RRE value for all profiles averaged was 36 % for the LMT calculation and 39 % for the UV+TIR and UV+TIR+MW measurements. Adding the MW measurement increased the RRE by 3 %. The DFS, PMS, and RRE values all show a certain increase in the retrieval sensitivity of the LMT ozone profile.

The sensitivity of MW measurement in the UT region largely depended on the atmospheric profile used, and this dependency was reflected in the wavelength combinations including the MW measurement. As shown in Fig. 3, the DFS values in the MW measurement for the UT in December for both areas were larger than those for June. The sensitivity of the MW measurements in the UT region increased for profiles with large amounts of the UT ozone. In the LMT, the DFS values of the UV and TIR measurements depended greatly on the atmospheric profiles. The average value of the partial column of ozone in the LMT region for CEC in June was 5.03×10^{21} m^{-2}, the largest among the four cases. Only the DFS value in the UV+TIR+MW for CEC in June was larger than unity (1.03±0.01).

More details of the vertical characteristics are discussed using the averaging kernel matrix A. Figures 5 and 6 show A and $\mathbf{m}$ obtained from the simulations using atmospheric profiles #01 and #12 for all wavelength combinations. The DFS values in the LMT for the UV+TIR+MW measurements of profiles #01 and #12 were respectively estimated to be 1.04 and 0.27, which were the highest and lowest values among the 20 profiles. For profile #01, the UV, TIR and MW measurements provided information on the LMT, the MT to UT, and the UT to the stratosphere, respectively. The UV and TIR measurements were important to retrieve the ozone amount in the LMT when only one wavelength range was used because their peaks in the row of A were located in the LMT region. The FWHM of the row of A for the UV and TIR measurements in the LMT was approximately 3 km. The peak value in the row of A increased from 0.25 for the UV and TIR measurements to 0.35 when the two measurements were combined. Combination of these measurements improves the sensitivity of retrieval of the LMT ozone

amount, as shown in the previous studies (Landgraf and Hasekamp, 2007; Worden et al., 2007; Natraj et al., 2011; Cuesta et al., 2013; Fu et al., 2013). Adding the MW measurement further increased it to 0.4. For profile #12 (less ozone in the LMT), the peak of the row of A for the UV measurement was located in the MT (maximum value of 0.1). Although the peak value in the MT increased to 0.23 as a result of combining the TIR and MW measurements, the peak value in the LMT remained low.

5 Additionally, we performed sensitivity study for the DFS, PMS and RRE using several σ_a values in order to obtain error volume. Figure 7 shows the DFS, PMS and RRE values with σ_a of 100 %, 50 %, 30 %, 20 % and 10 %. Here the calculation results for all 20 profiles were averaged. The DFS values decreased as the σ_a value decreased for all wavelength combinations considered in this study. This behavior was also observed for the RRE results. The PMS value seemed to locate in the corresponding vertical region when the σ_a value increased. The behavior of the relative differences of DFS, PMS and RRE for the 10 different wavelength combination was the same for all σ_a cases. Increase of retrieval sensitivity of the LMT ozone amount by adding the MW measurement was observed for all σ_a cases considered in this sensitivity study.

Our results show that introducing MW limb measurement increases the sensitivity of tropospheric ozone profile retrieval. However, several factors may cause bias and uncertainty in the retrieval results and thus should be considered before the proposed retrieval method is implemented. Discrepancy in the spectroscopic parameters for several wavelength ranges is a 15 major source of errors. For ozone profile retrieval using MW limb measurement, the spectroscopic parameters are the major error source. It was reported that an error of approximately 3–5 % was caused by uncertainties in the air-broadening coefficient and line intensity in the case of the SMILES observation (Kasai et al., 2013), which is comparable to the approximately 4 % uncertainty in the spectroscopic parameters in the UV and TIR wavelength ranges (Gratien et al., 2010). The tangent height correction can also be a large error source for the MW limb measurement (Kasai et al., 2013). The tangent height is a key 20 parameter to determine the field-of-view, so uncertainty in the tangent height causes a discrepancy between the atmospheric layer assumed in the simulation and the true atmospheric layer. This discrepancy critically affects the retrieval of the ozone profile in both the stratosphere and the troposphere, and may cause bias in the correction of the time delay between MW limb measurement and other nadir measurements. In this study, we assumed that the instruments onboard the ISS (low Earth orbit) and that a time difference of approximately five minutes could be ignored. If the time difference is actually long enough to 25 need correction, three-dimensional atmospheric modeling including the field-of-view of the MW limb measurement should be performed.

As a whole, it was shown that retrieval of the tropospheric ozone profile was improved by adding MW limb measurements to UV and TIR nadir measurements. In the LMT region, the DFS value was estimated to be increased by approximately 30 %. The DFS values were estimated to be 0.75 and 0.66 over land and ocean, respectively, for the upcoming IASI-NG and UVNS 30 missions (Constantino et al., 2017). If MW limb measurement is implemented to the synergetic retrieval, the DFS value is estimated to increase to 0.98 and 0.86 over land and ocean, respectively. Our feasibility study has shown that it is possible to retrieve the ozone profile in the LMT with a DFS value of unity.

5 Conclusions

We performed a feasibility study of obtaining vertically resolved ozone profiles in the troposphere with synergetic retrieval using various combinations of three wavelength ranges (UV, TIR, and MW). The observation geometries used in this study were the nadirs for the UV and TIR measurements and limb for the MW measurement from low Earth orbit (300 km, the height of the ISS). The urban (CEC) and ocean (ECS) area in June and December 2009 were assumed in this study. We evaluated the sensitivities of tropospheric ozone profile retrieval for the three vertical regions (UT (215–383 hPa), MT (383–749 hPa) and LMT (>749 hPa)) in terms of the degree of freedom for signal (DFS) based on the OEM calculation. The pressure of maximum sensitivity (PMS) and the reduction rate of error (RRE) for the partial column were also used as an indicator of the sensitivity evaluation.

The TIR measurement was most sensitive for retrieving the ozone profile in the UT when only one wavelength range was used. The addition of MW measurement was most effective at improving sensitivity in the UT when combining several wavelength ranges. The DFS values in the UT for all 20 profiles averaged were 0.62±0.08 and 1.21±0.28 for the UV+TIR and UV+TIR+MW measurements, respectively. In the MT region, the contribution of the TIR measurement was dominant in the DFS calculation. The average DFS value of the TIR measurement for all profiles averaged was 0.83±0.11. It was increased to more than unity by adding either the UV or MW measurement. The UV and TIR measurements were dominant in the retrieval of the ozone profile in the LMT region. The DFS value in the LMT greatly depended on the ozone abundance. It was larger for a larger partial column of the LMT ozone. The largest DFS value in the LMT for UV+TIR+MW measurement (1.03±0.01) was obtained for CEC in June which is the case with the largest LMT ozone enhancement with the partial column in the LMT ozone (approximately 5×10^{21} m^{-2}).

The MW limb measurement alone provided less information in the MT and LMT regions. The DFS values were less than 0.01 and the PMS was located in a vertical region higher than the MT and LMT. Nevertheless, adding MW measurement to the combined UV and TIR measurement improved sensitivity not only in the UT but also in the MT and LMT. The DFS values were increased by 96 %, 23 % and 30 % in the UT, MT and LMT, respectively, by adding the MW measurement to the UV+TIR measurement. This indicates that reducing uncertainty about ozone abundance in the stratosphere may be important for accurately estimating the tropospheric ozone profile.

References

Bak, J., Kim, J. H., Spurr, R. J. D., Liu, X. and Newchurch, M. J.: Sensitivity study of ozone retrieval from UV measurements on geostationary platforms, Remote Sensing of Environment, 118, 309–319, 2012.

Baldridge, A. M., Hook, S. J., Grove, C. I., and Rivera, G.: The ASTER spectral library version 2.0, Remote Sensing of Environment, 113, 711–715, 2009.

Baron, P., Mendrok, J., Kasai, Y., Ochiai, S., Seta, T., Sagi, K., Suzuki, K., Sagawa, H., and Urban, J.: AMATERAU: Model for atmospheric terahertz radiation analysis and simulation, Journal of National Institute of Information and Communications Technology, 55, 109–121, 2008.

Baron, P., Urban, J., Sagawa, H., Möller, J., Murtagh, D. P., Mendrok, J., Dupuy, E., Sato, T. O., Ochiai, S., Suzuki, K., Manabe, T., Nishibori, T., Kikuchi, K., Sato, R., Takayanagi, M., Murayama, Y., Shiotani, M., and Kasai, Y.: The Level 2 research product algorithms for the Superconducting Submillimeter-Wave Limb-Emission Sounder (SMILES), Atmospheric Measurement Techniques, 4, 2105–2124, doi:10.5194/amt-4-2105-2011, 2011.

Brinksma, E. J., Bracher, A., Lolkema, D. E., Segers, A. J., Boyd, I. S., Bramstedt, K., Claude, H., Godin-Beekmann, S., Hansen, G., Kopp, G., Leblanc, T., McDermid, I. S., Meijer, Y. J., Nakane, H., Parrish, A., von Savigny, C., Stebel, K., Swart, D. P. J., Taha, G. and Piters, A. J. M.: Geophysical validation of SCIAMACHY limb ozone profiles, Atmospheric Chemistry and Physics, 6, 197–209, 2006.

Clerbaux, C., Boynard, A., Clarisse, L., George, M., Hadji-Lazaro, J., Herbin, H., Hurtmans, D., Pommier, M., Razavi, A., Turquety, S., Wespes, C. and Coheur, P. F.: Monitoring of atmospheric composition using the thermal infrared IASI/MetOp sounder, Atmospheric Chemistry and Physics, 9, 6041–6054, 2009.

Clough, S. A., Shephard, M. W., Mlawer, E. J., Delamere, J. S., Iacono, M. J., Cady-Pereira, K., Boukabara, S., and Brown, P. D.: Atmospheric radiative transfer modeling: a summary of the AER codes, Journal of Quantitative Spectroscopy and Radiative Transfer, 91, 233–244, 2005.

Clough, S. A., Shephard, M. W., Worden, J., Brown, P. D., Worden, H. M., Luo, M., Rodgers, C. D., Rinsland, C. P., Goldman, A., Brown, L., Kulawik, S. S., Eldering, A., Lampel, M., Osterman, G., Beer, R., Bowman, K., Cady-Pereira, K. E., and Mlawer, E. J.: Forward model and Jacobians for tropospheric emission spectrometer retrievals, IEEE Transactions on Geoscience and Remote Sensing, 44, 1308–1323, 2006.

Costantino, L., Cuesta, J., Emili, E., Coman, A., Foret, G., Dufour, G., Eremenko, M., Chailleux, Y., Beekmann, M. and Flaud, J. M.: Potential of multispectral synergism for observing ozone pollution by combining IASI-NG and UVNS measurements from the EPS-SG satellite, Atmospheric Measurement Techniques, 10, 1281–1298, doi:10.5194/amt-10-1281-2017, 2017.

Cuesta, J., Eremenko, M., Liu, X., Dufour, G., Cai, Z., Höpfner, M., von Clarmann, T., Sellitto, P., Foret, G., Gaubert, B., Beekmann, M., Orphal, J., Chance, K., Spurr, R., and Flaud, J. M.: Satellite observation of lowermost tropospheric ozone by multispectral synergism of IASI thermal infrared and GOME-2 ultraviolet measurements over Europe, Atmospheric Chemistry and Physics, 13, 9675–9693, 2013.

Dentener, F., Keating, T., and Akimoto, H.: Hemispheric transport of air pollution, United Nations, ISBN, pp. 978–992, 2010.

Fleming, E. L., Chandra, S., Schoeberl, M. R. and Barnett, J. J.: Monthly mean global climatology of temperature, wind, geopotential height, and pressure for 0–120 km, NASA Tech Memo 100687, 85, 1988.

Fleming, E. L., Chandra, S., Barnett, J. J., and Corney, M.: Zonal mean temperature, pressure, zonal wind and geopotential height as functions of latitude, Advances in Space Research, 10, 11–59, 1990.

Fu, D., Worden, J. R., Liu, X., Kulawik, S. S., Bowman, K. W., and Natraj, V.: Characterization of ozone profiles derived from Aura TES and OMI radiances, Atmospheric Chemistry and Physics, 13, 3445–3462, 2013.

Fujinawa, T., Kasai, Y., Mahani, M., uvSCOPE team and APOLLO mission team: Japanese future mission for air quality uvSCOPE and APOLLO, 8th Atmospheric Limb workshop Abstracts, 2015.

5 Gratien, A., Picquet-Varrault, B., Orphal, J., Doussin, J. F., and Flaud, J. M.: New Laboratory Intercomparison of the Ozone Absorption Coefficients in the Mid-infrared (10 μm) and Ultraviolet (300–350 nm) Spectral Regions, The Journal of Physical Chemistry A, 114(37), 10045–10048, doi:10.1021/jp103992f, 2010.

Grell, G. A., Peckham, S. E., Schmitz, R., McKeen, S. A., Frost, G., Skamarock, W. C. and Eder, B.: Fully coupled "online" chemistry within the WRF model, Atmospheric Environment, 39, 6957–6975, 2005.

10 Hayashida, S., Liu, X., Ono, A., Yang, K., and Chance, K.: Observation of ozone enhancement in the lower troposphere over East Asia from a space-borne ultraviolet spectrometer, Atmospheric Chemistry and Physics, 15(17), 9865–9881, doi:10.5194/acp-15-9865-2015, 2015.

Hess, M., Koepke, P., and Schult, I.: Optical properties of aerosols and clouds: The software package OPAC, Bulletin of the American meteorological society, 79, 831–844, 1998.

Kasai, Y., Kita, K., Kanaya, Y., Gmap-Asia and Apollo Mission Team: The Japanese Air Pollusion Observation Missions, GMAP-Asia and
15 APOLLO, AGU Fall Meeting Abstracts, 2011.

Kasai, Y., Sagawa, H., Kuroda, T., Manabe, T., Ochiai, S., Kikuchi, K., Nishibori, T., Baron, P., Mendrok, J., Hartogh, P., Murtagh, D., Urban, J., von Schéele, F., and Frisk, U.: Overview of the Martian atmospheric submillimetre sounder FIRE, Planetary and Space Science, 63, 62–82, 2012.

Kasai, Y., Sagawa, H., Kreyling, D., Dupuy, E., Baron, P., Mendrok, J., Suzuki, K., Sato, T. O., Nishibori, T., Mizobuchi, S., Kikuchi, K.,
20 Manabe, T., Ozeki, H., Sugita, T., Fujiwara, M., Irimajiri, Y., Walker, K. A., Bernath, P. F., Boone, C., Stiller, G., von Clarmann, T., Orphal, J., Urban, J., Murtagh, D., Llewellyn, E. J., Degenstein, D., Bourassa, A. E., Lloyd, N. D., Froidevaux, L., Birk, M., Wagner, G., Schreier, F., Xu, J., Vogt, P., Trautmann, T., and Yasui, M.: Validation of stratospheric and mesospheric ozone observed by SMILES from International Space Station, Atmospheric Measurement Techniques, 6, 2311–2338, doi:10.5194/amt-6-2311-2013, 2013.

Kikuchi, K., Nishibori, T., Ochiai, S., Ozeki, H., Irimajiri, Y., Kasai, Y., Koike, M., Manabe, T., Mizukoshi, K., Murayama, Y., Nagahama,
25 T., Sano, T., Sato, R., Seta, M., Takahashi, C., Takayanagi, M., Masuko, H., Inatani, J., Suzuki, M., and Shiotani, M.: Overview and early results of the Superconducting Submillimeter-Wave Limb-Emission Sounder (SMILES), Journal of Geophysical Research: Atmospheres, 115, D23306, doi:10.1029/2010JD014379, 2010.

Kleipool, Q. L., Dobber, M. R., de Haan, J. F., and Levelt, P. F.: Earth surface reflectance climatology from 3 years of OMI data, Journal of Geophysical Research: Atmospheres, 113, 2008.

30 Kyrölä, E., Tamminen, J., Leppelmeier, G. W., Sofieva, V., Hassinen, S., Bertaux, J. L., Hauchecorne, A., Dalaudier, F., Cot, C., Korablev, O., Fanton d'Andon, O., Barrot, G., Mangin, A., Théodore, B., Guirlet, M., Etanchaud, F., Snoeij, P., Koopman, R., Saavedra, L., Fraisse, R., Fussen, D. and Vanhellemont, F.: GOMOS on Envisat: An overview, Advances in Space Research, 33, 1020–1028, 2004.

Landgraf, J., and Hasekamp, O. P.: Retrieval of tropospheric ozone: The synergistic use of thermal infrared emission and ultraviolet reflectivity measurements from space, Journal of Geophysical Research: Atmospheres, 112, 2007.

35 Levelt, P. F., van den Oord, G. H. J., Dobber, M. R., Malkki, A., Visser, H., de Vries, J., Stammes, P., Lundell, J. O. V., and Saari, H.: The ozone monitoring instrument, IEEE Transactions on geoscience and remote sensing, 44, 1093–1101, 2006.

Munro, R., Eisinger, M., Anderson, C., Callies, J., Corpaccioli, E., Lang, R., Lefebvre, A., Livschitz, Y., and Albinana, A. P.: GOME-2 on MetOp, in: Proc. of The 2006 EUMETSAT Meteorological Satellite Conference, Helsinki, Finland, pp. 12–16, 2006.

Natraj, V., Liu, X., Kulawik, S., Chance, K., Chatfield, R., Edwards, D. P., Eldering, A., Francis, G., Kurosu, T., Pickering, K., Spurr, R. and Worden, H.: Multi-spectral sensitivity studies for the retrieval of tropospheric and lowermost tropospheric ozone from simulated clear-sky GEO-CAPE measurements, Atmospheric Environment, 45, 7151–7165, 2011.

Noguchi, K., Richter, A., Rozanov, V., Rozanov, A., Burrows, J. P., Irie, H., and Kita, K.: Effect of surface BRDF of various land cover types on geostationary observations of tropospheric NO_2, Atmospheric Measurement Techniques, 7, 3497–3508, 2014.

Osterman, G. B., Kulawik, S. S., Worden, H. M., Richards, N. A. D., Fisher, B. M., Eldering, A., Shephard, M. W., Froidevaux, L., Labow, G., Luo, M., Herman, R. L., Bowman, K. W., and Thompson, A. M.: Validation of Tropospheric Emission Spectrometer (TES) measurements of the total, stratospheric, and tropospheric column abundance of ozone, Journal of Geophysical Research: Atmospheres, 113, 2008.

Pardo, J. R., Serabyn, E., and Cernicharo, J.: Submillimeter atmospheric transmission measurements on Mauna Kea during extremely dry El Niño conditions: Implications for broadband opacity contributions, Journal of Quantitative Spectroscopy and Radiative Transfer, 68, 419–433, 2001.

Pickett, H. M., Poynter, R. L., Cohen, E. A., Delitsky, M. L., Pearson, J. C., and Müller, H. S. P.: Submillimeter, millimeter and microwave spectral line catalog, Journal of Quantitative Spectroscopy and Radiative Transfer, 60, 883–890, doi:10.1016/S0022-4073(98)00091-0, 1998.

Rienecker, M. M., Suarez, M. J., Gelaro, R., Todling, R., Bacmeister, J., Liu, E., Bosilovich, M. G., Schubert, S. D., Takacs, L., Kim, G. K., Bloom, S., Chen, J., Collins, D., Conaty, A., da Silva, A., Gu, W., Joiner, J., Koster, R. D., Lucchesi, R., Molod, A., Owens, T., Pawson, S., Pegion, P., Redder, C. R., Reichle, R., Robertson, F. R., Ruddick, A. G., Sienkiewicz, M., and Woollen, J.: MERRA: NASA's modern-era retrospective analysis for research and applications, Journal of Climate, 24, 3624–3648, 2011.

Rodgers, C. D.: Inverse methods for atmospheric sounding: Theory and practice, Series on Atmospheric, Oceanic and Planetary Physics, World Scientific, 2, 3605–3609, 2000.

Rothman, L. S., Gordon, I. E., Barbe, A., Benner, D. C., Bernath, P. F., Birk, M., Boudon, V., Brown, L. R., Campargue, A., Champion, J. P., Chance, K., Coudert, L. H., Dana, V., Devi, V. M., Fally, S., Flaud, J. M., Gamache, R. R., Goldman, A., Jacquemart, D., Kleiner, I., Lacome, N., Lafferty, W. J., Mandin, J. Y., Massie, S. T., Mikhailenko, S. N., Miller, C. E., Moazzen-Ahmadi, N., Naumenko, O. V., Nikitin, A. V., Orphal, J., Perevalov, V. I., Perrin, A., Predoi-Cross, A., Rinsland, C. P., Rotger, M., Šimečková, M., Smith, M. A. H., Sung, K., Tashkun, S. A., Tennyson, J., Toth, R. A., Vandaele, A. C., and Vander Auwera, J.: The HITRAN 2008 molecular spectroscopic database, Journal of Quantitative Spectroscopy and Radiative Transfer, 110, 533–572, doi:10.1016/j.jqsrt.2009.02.013, 2009.

Rozanov, A., Rozanov, V., Buchwitz, M., Kokhanovsky, A., and Burrows, J. P.: SCIATRAN 2.0–A new radiative transfer model for geophysical applications in the 175–2400 nm spectral region, Advances in Space Research, 36, 1015–1019, 2005.

Saitoh, N., Imasu, R., Ota, Y., and Niwa, Y.: CO_2 retrieval algorithm for the thermal infrared spectra of the Greenhouse Gases Observing Satellite: Potential of retrieving CO_2 vertical profile from high-resolution FTS sensor, Journal of Geophysical Research: Atmospheres, 114, D17305, doi:10.1029/2008JD011500, 2009.

Sellitto, P., Del Frate, F., Solimini, D., and Casadio, S.: Tropospheric ozone column retrieval from ESA-Envisat SCIAMACHY nadir UV/VIS radiance measurements by means of a neural network algorithm, IEEE Transactions on Geoscience and Remote Sensing, 50, 998–1011, doi:10.1109/TGRS.2011.2163198, 2012a.

Sellitto, P., Di Noia, A., Del Frate, F., Burini, A., Casadio, S., and Solimini, D.: On the role of visible radiation in ozone profile retrieval from nadir UV/VIS satellite measurements: An experiment with neural network algorithms inverting SCIAMACHY data, Journal of Quantitative Spectroscopy and Radiative Transfer, 113, 1429–1436, doi:10.1016/j.jqsrt.2012.04.007, 2012b.

Sudo, K., Takahashi, M., Kurokawa, J., and Akimoto, H.: CHASER: A global chemical model of the troposphere 1. Model description, Journal of Geophysical Research: Atmospheres, 107, 2002.

Takigawa, M., Niwano, M., Akimoto, H., and Takahashi, M.: Development of a one-way nested global-regional air quality forecasting model, Sola, 3, 81–84, 2007.

5 Takigawa, M., Niwano, M., Akimoto, H., Takahashi, M., and Kobayashi, K.: Projection of surface ozone over East Asia in 2020, Journal of Agriculture Meteorology, 65, 161–166, 2009.

Urban, J., Lautié, N., Le Flochmoën, E., Jiménez, C., Eriksson, P., de La Noë, J., Dupuy, E., Ekström, M., El Amraoui, L., Frisk, U., Murtagh, D., Olberg, M., and Ricaud, P.: Odin/SMR limb observations of stratospheric trace gases: Level 2 processing of ClO, N_2O, HNO_3, and O_3, Journal of Geophysical Research: Atmospheres, 110, 2005.

10 Waters, J. W., Froidevaux, L., Harwood, R. S., Jarnot, R. F., Pickett, H. M., Read, W. G., Siegel, P. H., Cofield, R. E., Filipiak, M. J., Flower, D. A., Holden, J. R., Lau, G. K., Livesey, N. J., Manney, G. L., Pumphrey, H. C., Santee, M. L., Wu, D. L., Cuddy, D. T., Lay, R. R., Loo, M. S., Perun, V. S., Schwartz, M. J., Stek, P. C., Thurstans, R. P., Boyles, M. A., Chandra, K. M., Chavez, M. C., Chen, G. S., Chudasama, B. V., Dodge, R., Fuller, R. A., Girard, M. A., Jiang, J. H., Jiang, Y., Knosp, B. W., LaBelle, R. C., Lam, J. C., Lee, K. A., Miller, D., Oswald, J. E., Patel, N. C., Pukala, D. M., Quintero, O., Scaff, D. M., Snyder, W. V., Tope, M. C., Wagner, P. A., and Walch, M. J.:

15 The earth observing system microwave limb sounder (EOS MLS) on the Aura satellite, IEEE Transactions on Geoscience and Remote Sensing, 44, 1075–1092, 2006.

WHO: Burden of disease from Ambient Air Pollution for 2012, Geneva: World Health Organization, 2014.

Worden, J., Liu, X., Bowman, K., Chance, K., Beer, R., Eldering, A., Gunson, M., and Worden, H.: Improved tropospheric ozone profile retrievals using OMI and TES radiances, Geophysical Research Letters, 34, 2007.

20 Ziemke, J. R., Chandra, S., Duncan, B. N., Froidevaux, L., Bhartia, P. K., Levelt, P. F., and Waters, J. W.: Tropospheric ozone determined from Aura OMI and MLS: Evaluation of measurements and comparison with the Global Modeling Initiative's Chemical Transport Model, Journal of Geophysical Research: Atmospheres, 111, 2006.
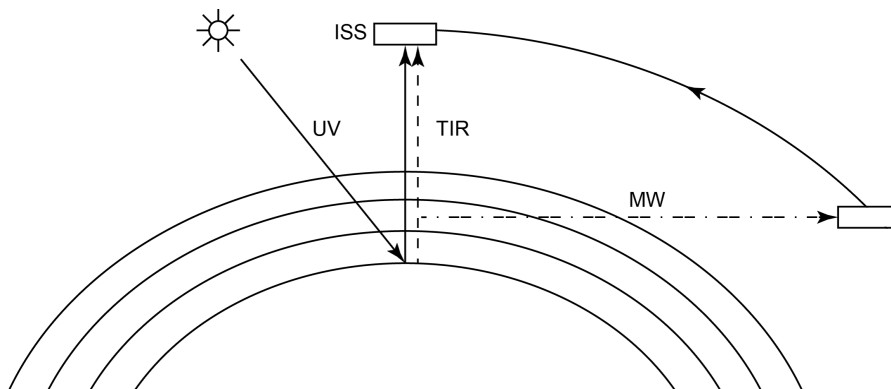
Figure 1. Geometries used for observation: nadir (UV and TIR) and limb (MW).

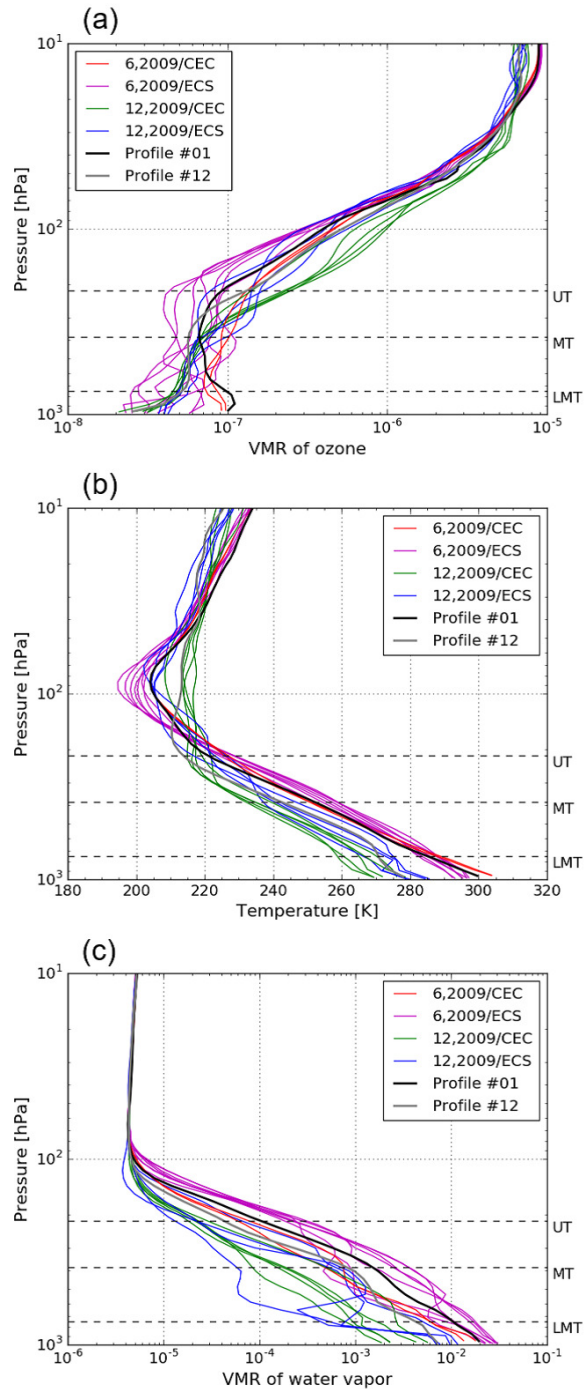**Figure 2.** Twenty atmospheric scenarios used in this study: (a) VMR of ozone, (b) temperature, and (c) VMR of water vapor. They are divided into four groups, as denoted by color: CEC–June 2009 (red), ECS-June 2009 (purple), CEC–December 2009 (green), and ECS–December 2009 (blue). Two example profiles (#01 and #12, black and gray lines, respectively) were used to obtain results shown in Figs. 5 and 6.

Figure 3. Values of DFS for upper troposphere (UT, 215–383 hPa), middle troposphere (MT, 383–749 hPa), and lowermost troposphere (LMT, >749 hPa): CEC–June 2009 (red), ECS–June 2009 (purple), CEC–December 2009 (green), ECS–December 2009 (blue), and 20 profiles averaged (black).
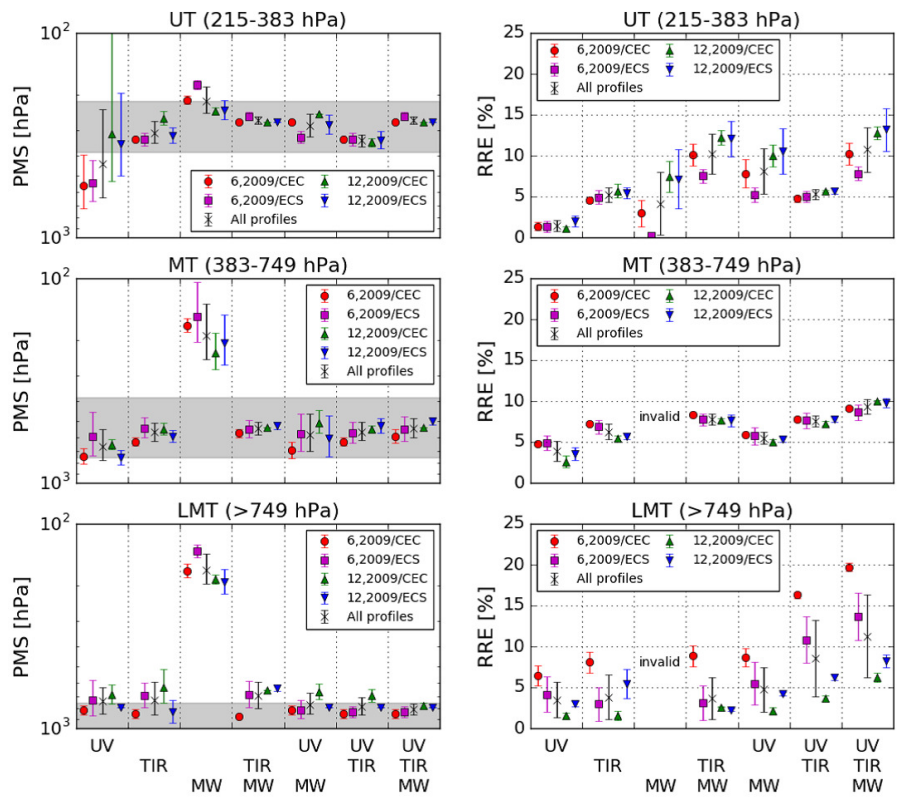
Figure 4. Same as Fig. 3 but for the PMS (left) and RRE (right). The gray shaded area represents the vertical region that corresponds to UT, MT and LMT.
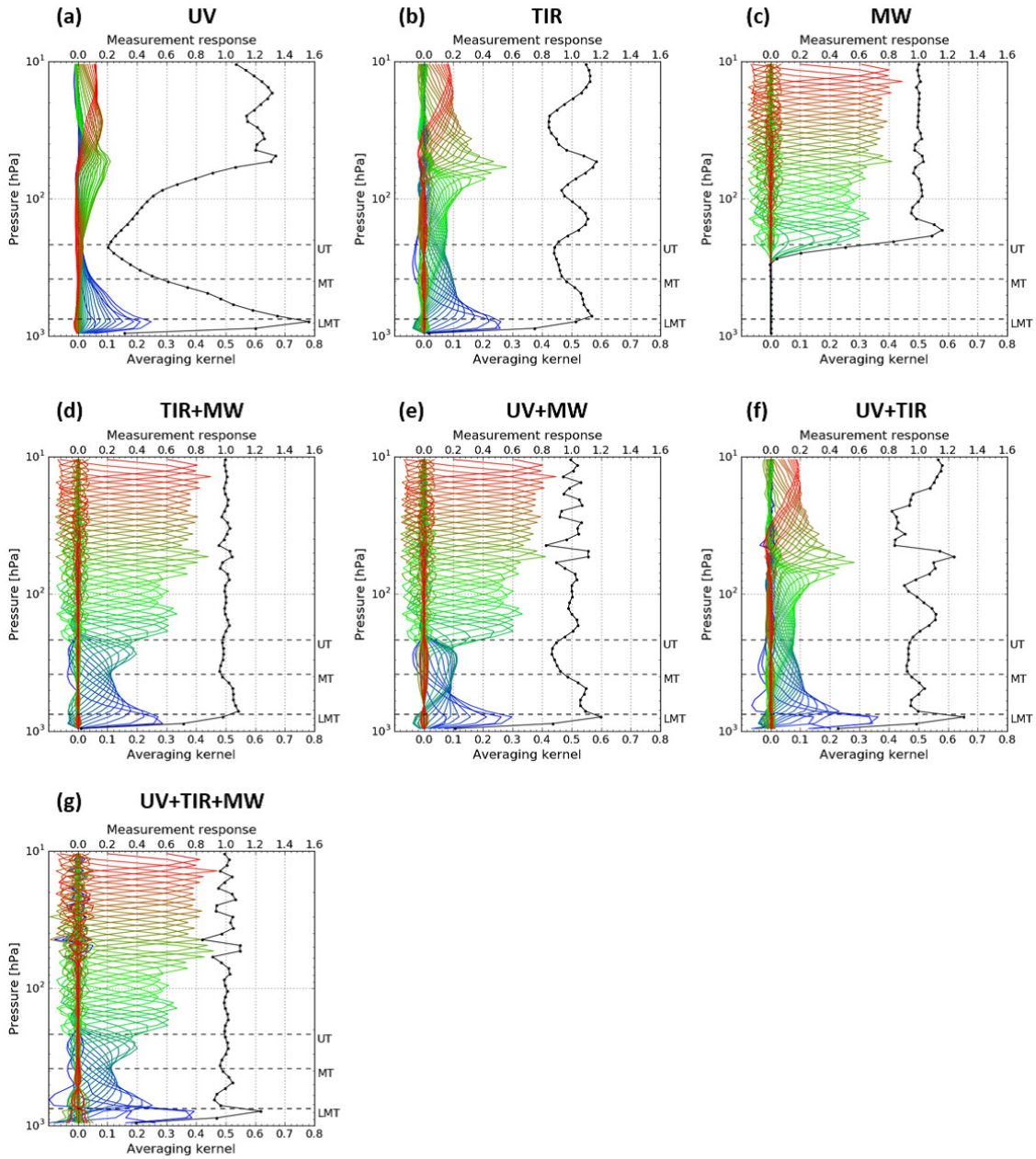
Figure 5. Averaging kernels for atmospheric profile #01 (more ozone enhancement in LMT, CEC–June 2009) for seven wavelength measurements: (a) UV, (b) TIR, (c) MW, (d) UV+TIR, (e) UV+MW, (f) TIR+MW, and (g) UV+TIR+MW. Measurement responses are shown by black dots and lines.
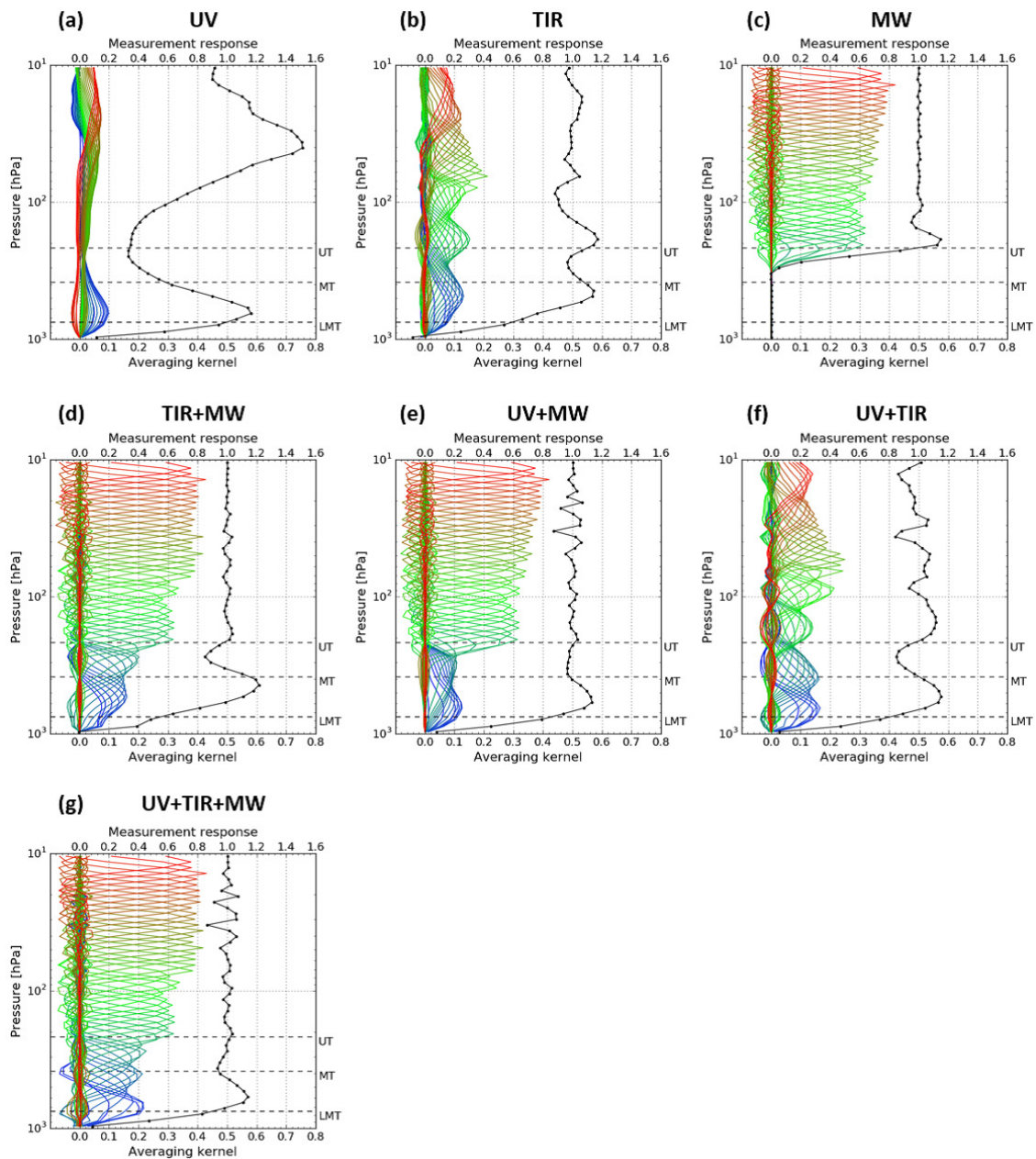
Figure 6. Same as Fig. 5 but for profile #12 (less ozone in LMT, CEC–December 2009).
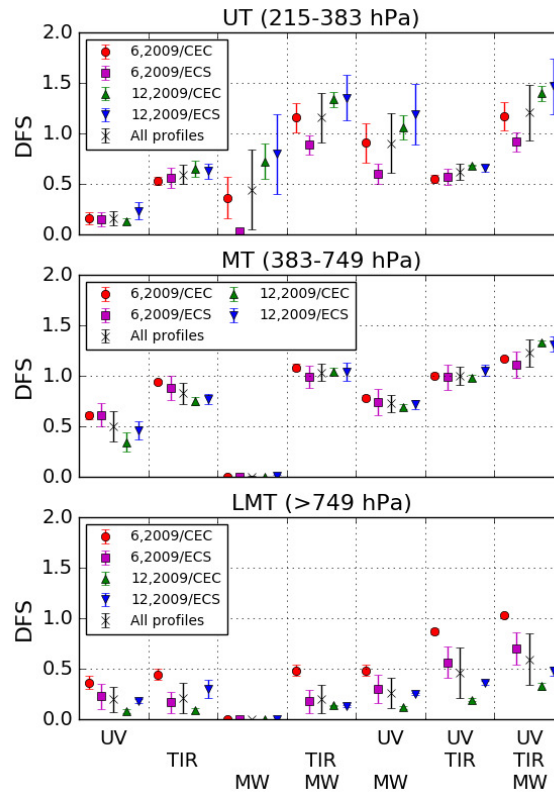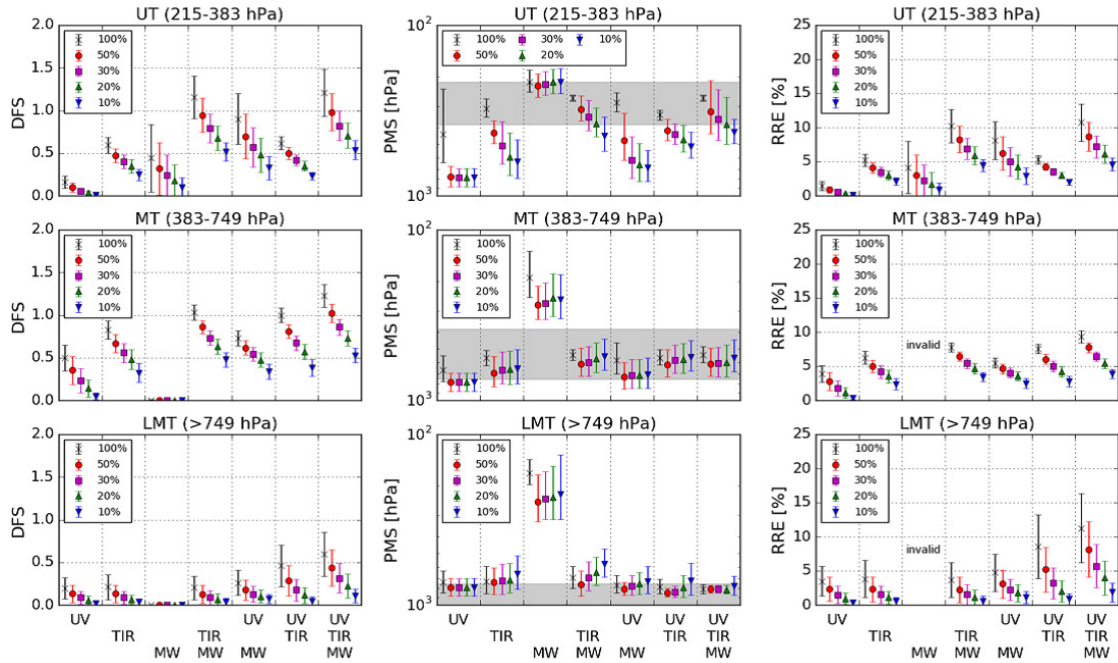
Figure 7. Values of DFS, PMS and RRE for upper troposphere (UT, 215–383 hPa), middle troposphere (MT, 383–749 hPa), and lowermost troposphere (LMT, >749 hPa) for 20 profiles averaged: σ_a values of 100 % (black), 50 % (red), 30 % (purple), 20 % (green) and 10 % (blue) of the log-based a priori VMR.

Table 1. Specifications of three assumed instruments and radiative transfer models.

	UV	TIR	MW
Observation geometry	Nadir-viewing	Nadir-viewing	Limb-viewing
Wavelength	305–340 nm	980–1080 cm^{-1}	345–357 GHz, 639–651 GHz
Spectral resolution	0.6 nm	~0.12 cm^{-1}	25 MHz
Sampling step	0.2 nm	~0.12 cm^{-1}	25 MHz
Sensitivity[a]	90 (305 nm)–1400 (340 nm)	300	0.7 K (350 GHz band), 1.7 K (645 GHz band)
Scattering	Yes	No	No
Emission	No	Yes	Yes
Forward model	SCIATRAN	LBLRTM	AMATERASU

[a] Instrument sensitivity is described in commonly used way for each spectral region: SNR for UV and TIR and noise equivalent brightness temperature for MW.

Table 2. Estimation of three reference SNR value in the UV simulation.

	SNR at 305 nm	SNR at 340 nm
Case 1: high level radiance (albedo 90 %, SZA 0°)	~200	~2550
Case 2: middle level radiance (albedo 25 %, SZA 45°)	~60	~1200
Case 3: low level radiance (albedo 5 %, SZA 80°)	~10	~450

Table 3. Summary of 20 atmospheric scenarios used in the simulation.

#	Date[a]	Area[b]	$T_s{}^c$ [K]	$P_s{}^c$ [hPa]	PC (UT)[d] [m^{-2}]	PC (MT)[d] [m^{-2}]	PC (LMT)[d] [m^{-2}]	H_2O[e] [g/cm^2]
01	6/16	CEC	301.4	976.0	2.57×10^{21}	5.87×10^{21}	5.66×10^{21}	3.4
02	6/24	CEC	304.5	970.2	4.13×10^{21}	6.14×10^{21}	4.51×10^{21}	2.1
03	6/25	CEC	305.0	970.2	3.65×10^{21}	6.52×10^{21}	4.93×10^{21}	2.3
04	6/3	ECS	293.9	999.6	1.49×10^{21}	4.39×10^{21}	3.72×10^{21}	4.5
05	6/9	ECS	294.9	1010.9	1.68×10^{21}	4.17×10^{21}	3.96×10^{21}	4.2
06	6/20	ECS	296.0	1004.2	2.92×10^{21}	6.34×10^{21}	1.86×10^{21}	3.7
07	6/21	ECS	296.5	1002.9	3.00×10^{21}	4.26×10^{21}	2.39×10^{21}	6.0
08	6/26	ECS	296.8	1010.0	3.27×10^{21}	6.20×10^{21}	2.25×10^{21}	4.1
09	6/27	ECS	297.6	1006.6	2.13×10^{21}	3.13×10^{21}	1.49×10^{21}	6.0
10	6/30	ECS	298.1	1004.5	2.71×10^{21}	3.05×10^{21}	1.80×10^{21}	5.9
11	12/2	CEC	280.7	993.1	3.20×10^{21}	4.47×10^{21}	1.83×10^{21}	1.1
12	12/11	CEC	280.0	988.8	2.66×10^{21}	4.38×10^{21}	2.10×10^{21}	1.4
13	12/20	CEC	271.6	997.3	4.58×10^{21}	4.14×10^{21}	2.22×10^{21}	0.3
14	12/22	CEC	278.1	985.9	4.25×10^{21}	4.27×10^{21}	2.21×10^{21}	0.6
15	12/27	CEC	271.3	992.6	4.51×10^{21}	4.41×10^{21}	2.10×10^{21}	0.4
16	12/28	CEC	274.0	985.8	4.12×10^{21}	4.33×10^{21}	2.15×10^{21}	0.4
17	12/4	ECS	286.7	1019.2	4.04×10^{21}	4.48×10^{21}	2.54×10^{21}	1.1
18	12/12	ECS	287.9	1019.9	2.35×10^{21}	4.81×10^{21}	2.92×10^{21}	2.0
19	12/21	ECS	282.4	1025.7	4.91×10^{21}	4.74×10^{21}	2.68×10^{21}	0.8
20	12/26	ECS	281.3	1019.3	3.72×10^{21}	4.38×10^{21}	2.68×10^{21}	0.9

[a] All simulation data are from 2009.

[b] CEC and ECS stand for Central East China (30°N–40°N, 110°E–123°E) and the East China Sea (29°N–33°N, 125°E–129.5°E), respectively.

[c] Temperature and pressure at the surface.

[d] PC means ozone partial column. PC is presented for each altitude region: upper troposphere (UT, 215–383 hPa), middle troposphere (MT, 383–749 hPa), and lowermost troposphere (LMT, > 749 hPa).

[e] H_2O column amount in the troposphere.

Table 4. Mean and standard deviation (1-σ) of DFS in the upper troposphere (UT, 215–383 hPa), middle troposphere (MT, 383–749 hPa), and lowermost troposphere (LMT, >749 hPa). Standard deviation is shown in parentheses. For example, 0.16(6) represents a mean value of 0.16 and a standard deviation of 0.06.

		UV	TIR	MW	TIR+MW	UV+MW	UV+TIR	UV+TIR+MW
6, 2009/CEC	UT	0.16(6)	0.53(4)	0.36(20)	1.16(14)	0.91(20)	0.55(4)	1.17(14)
	MT	0.61(3)	0.94(2)	<0.01	1.08(4)	0.78(3)	1.00(2)	1.17(1)
	LMT	0.37(6)	0.44(6)	<0.01	0.48(6)	0.48(5)	0.87(3)	1.03(1)
6, 2009/ECS	UT	0.15(7)	0.56(10)	0.03(3)	0.89(9)	0.60(10)	0.57(8)	0.92(10)
	MT	0.61(11)	0.88(12)	<0.01	0.99(11)	0.74(13)	0.99(13)	1.11(13)
	LMT	0.23(13)	0.17(11)	<0.01	0.18(11)	0.30(14)	0.56(15)	0.70(16)
12, 2009/CEC	UT	0.12(3)	0.65(8)	0.72(17)	1.34(8)	1.06(12)	0.68(1)	1.40(7)
	MT	0.34(9)	0.75(4)	<0.01	1.04(3)	0.69(2)	0.98(3)	1.33(2)
	LMT	0.08(2)	0.09(3)	<0.01	0.14(1)	0.12(2)	0.19(1)	0.33(3)
12, 2009/ECS	UT	0.23(8)	0.63(8)	0.80(40)	1.35(23)	1.19(30)	0.66(4)	1.47(27)
	MT	0.46(9)	0.77(5)	<0.01	1.04(9)	0.72(5)	1.05(5)	1.31(7)
	LMT	0.18(2)	0.30(9)	<0.01	0.13(1)	0.25(1)	0.36(2)	0.48(5)
All profiles	UT	0.16(7)	0.59(9)	0.44(40)	1.16(25)	0.90(30)	0.62(8)	1.21(28)
	MT	0.50(15)	0.83(11)	<0.01	1.03(8)	0.73(9)	1.00(9)	1.23(13)
	LMT	0.20(12)	0.21(15)	<0.01	0.20(14)	0.26(15)	0.46(25)	0.59(26)

Table 5. Comparison of DFS in the LMT region with those of previous studies. Method and scenarios differed, so relative difference between DFS value for UV+TIR measurement (DFS_{UV+TIR}) and mean of DFS values for UV and TIR measurements (DFS_{UV}, DFS_{TIR}) was used for comparison. The relative difference was calculated by (DFS_{UV+TIR} − Mean(DFS_{UV}, DFS_{TIR}))/Mean(DFS_{UV}, DFS_{TIR}).

	DFS_{UV}	DFS_{TIR}	Mean(DFS_{UV}, DFS_{TIR})	DFS_{UV+TIR}	Rel. dif.	Definition of LMT
This work	0.20	0.21	0.203	0.458	126 %	>749 hPa
Fu et al. (2013)	0.10	0.21	0.15	0.37	139 %	>700 hPa
Cuesta et al. (2013)[a]	0.08	0.20	0.14	0.285	104 %	<3 km
Natraj et al. (2011)	0.26	0.27	0.265	0.57	115 %	>800 hPa

[a] DFS values over land and ocean are averaged.